City Research Online

City, University of London Institutional Repository

Citation: Kloepfer, D., De Martino, A. & Egger, R. (2013). Bound States and Supercriticality in Graphene-Based Topological Insulators. Crystals, 3(1), pp. 14-27. doi: 10.3390/cryst3010014

This is the published version of the paper.

This version of the publication may differ from the final published version.

Permanent repository link: https://openaccess.city.ac.uk/id/eprint/4428/

Link to published version: https://doi.org/10.3390/cryst3010014

Copyright: City Research Online aims to make research outputs of City, University of London available to a wider audience. Copyright and Moral Rights remain with the author(s) and/or copyright holders. URLs from City Research Online may be freely distributed and linked to.

Reuse: Copies of full items can be used for personal research or study, educational, or not-for-profit purposes without prior permission or charge. Provided that the authors, title and full bibliographic details are credited, a hyperlink and/or URL is given for the original metadata page and the content is not changed in any way.

City Research Online: http://openaccess.city.ac.uk/ publications@city.ac.uk

Crystals **2013**, *3*, 14-27; doi:10.3390/cryst3010014

OPEN ACCESS

crystals

ISSN 2073-4352

www.mdpi.com/journal/crystals

Article

Bound States and Supercriticality in Graphene-Based Topological Insulators

Denis Klöpfer [1], Alessandro De Martino [2] and Reinhold Egger [1,]*

[1] Institut für Theoretische Physik, Heinrich-Heine-Universität, D-40225 Düsseldorf, Germany;
E-Mail: kloepfer@thphy.uni-duesseldorf.de

[2] Department of Mathematical Science, City University London, London EC1V 0HB, UK;
E-Mail: ademarti@city.ac.uk

* Author to whom correspondence should be addressed; E-Mail: egger@thphy.uni-duesseldorf.de;
Tel.: +49-211-81-14710; Fax:+49-211-81-15630.

Received: 16 November 2012; in revised form: 17 December 2012 / Accepted: 9 January 2013 /
Published: 21 January 2013

Abstract: We study the bound state spectrum and the conditions for entering a supercritical regime in graphene with strong intrinsic and Rashba spin-orbit interactions within the topological insulator phase. Explicit results are provided for a disk-shaped potential well and for the Coulomb center problem.

Keywords: graphene; supercriticality; spin-orbit interaction

---

1. Introduction

The electronic properties of graphene monolayers are presently under intense study. Previous works have already revealed many novel and fundamental insights; for reviews, see [1,2]. Following the seminal work of Kane and Mele [3], it may be possible to engineer a two-dimensional (2D) topological insulator (TI) phase [4] in graphene by enhancing the—usually very weak [5–7]—spin-orbit interaction (SOI) in graphene. This enhancement could, for instance, be achieved by the deposition of suitable adatoms [8]. Remarkably, random deposition should already be sufficient to reach the TI phase [9–11] where the effective "intrinsic" SOI Δ exceeds (half of) the "Rashba" SOI λ. So far, the only 2D TIs realized experimentally are based on the mercury telluride class. Using graphene as a TI material constitutes a very attractive option because of the ready availability of high-quality graphene samples [1] and the exciting prospects for stable and robust TI-based devices [4], see also [12,13].

In this work, we study bound-state solutions and the conditions for supercriticality in a graphene-based TI. Such questions can arise in the presence of an electrostatically generated potential well ("quantum dot") or for a Coulomb center. The latter case can be realized by artificial alignment of Co trimers [14], or when defects or charged impurities reside in the graphene layer. Without SOI, the Coulomb impurity problem in graphene has been theoretically studied in depth [15–20]; for reviews, see [1,2]. Moreover, for $\lambda = 0$, an additional mass term in the Hamiltonian corresponds to the intrinsic SOI Δ (see below), and the massive Coulomb impurity problem in graphene has been analyzed in [21–26]. However, a finite Rashba SOI λ is inevitable in practice and has profound consequences. In particular, $\lambda \neq 0$ breaks electron-hole symmetry and modifies the structure of the vacuum. We therefore address the general case with both Δ and λ finite, but within the TI phase $\Delta > \lambda/2$, in this paper. Experimental progress on the observation of Dirac quasiparticles near a Coulomb impurity in graphene was also reported very recently [14], and we are confident that the topological version with enhanced SOI can be studied experimentally in the near future. Our work may also be helpful in the understanding of spin-orbit mediated spin relaxation in graphene [27].

The atomic collapse problem for Dirac fermions in an attractive Coulomb potential, $V(r) = -\hbar v_F \alpha/r$, could thereby be realized in topological graphene. Here we use the dimensionless impurity strength

$$\alpha = \frac{Ze^2}{\kappa \hbar v_F} \simeq 2.2 \frac{Z}{\kappa} \tag{1}$$

where Z is the number of positive charges held by the impurity; κ a dielectric constant characterizing the environment; and $v_F \approx 10^6$ m/s the Fermi velocity. Without SOI, the Hamiltonian is not self-adjoint for $\alpha > \alpha_c = 1/2$, and the potential needs short-distance regularization, e.g., by setting $V(r < R) = -\hbar v_F \alpha/R$ with short-distance cutoff R of the order of the lattice constant of graphene [1,2]. Including a finite "mass" Δ, *i.e.*, the intrinsic SOI, but keeping $\lambda = 0$, the critical coupling α_c is shifted to [24]

$$\alpha_c \simeq \frac{1}{2} + \frac{\pi^2}{\ln^2(0.21\Delta R/\hbar v_F)} \tag{2}$$

approaching the value $\alpha_c = 1/2$ for $R \to 0$. In the supercritical regime $\alpha > \alpha_c$, the lowest bound state "dives" into the valence band continuum (Dirac sea). It then becomes a resonance with complex energy, where the imaginary part corresponds to the finite decay rate into the continuum. Below we show that the Rashba SOI provides an interesting twist to this supercriticality story. The structure of this article is as follows. In Section 2 we introduce the model and summarize its symmetries. The case of a circular potential well is addressed in Section 3 before turning to the Coulomb center in Section 4. Some conclusions are offered in Section 5. Note that we do not include a magnetic field (see, e.g., [28,29]) and thus our model enjoys time-reversal symmetry. Below, we often use units with $\hbar = v_F = 1$.

2. Model and Symmetries

2.1. Kane–Mele Model with Radially Symmetric Potential

We study the Kane–Mele model for a 2D graphene monolayer with both intrinsic (Δ) and Rashba (λ) SOI [3] in the presence of a radially symmetric scalar potential $V(r)$. Assuming that $V(r)$ is sufficiently smooth to allow for the neglect of inter-valley scattering, the low-energy Hamiltonian near the K point ($\tau = +1$) is given by

$$H = \tau\sigma_x p_x + \sigma_y p_y + \tau\Delta\sigma_z s_z + \frac{\lambda}{2}(\tau\sigma_x s_y - \sigma_y s_x) + V(r) \tag{3}$$

with Pauli matrices $\sigma_{x,y,z}$ ($s_{x,y,z}$) in sublattice (spin) space [1]. The Hamiltonian near the other valley (K' point) follows for $\tau = -1$ in Equation (3). We note that a sign change of the Rashba SOI, $\lambda \to -\lambda$, does not affect the spectrum due to the relation $H(-\lambda) = s_z H(\lambda) s_z$. Without loss of generality, we then put $\Delta \geq 0$ and $\lambda \geq 0$.

Using polar coordinates, it is now straightforward to verify (see also [21]) that total angular momentum, defined as

$$J_z = -i\partial_\phi + s_z/2 + \tau\sigma_z/2 \tag{4}$$

is conserved and has integer eigenvalues j. For given j, eigenfunctions of H must then be of the form

$$\Psi_{j,\tau=+}(r,\phi) = \begin{pmatrix} e^{i(j-1)\phi}\, a_{\uparrow,j,+}(r) \\ ie^{ij\phi}\, b_{\uparrow,j,+}(r) \\ e^{ij\phi}\, a_{\downarrow,j,+}(r) \\ ie^{i(j+1)\phi}\, b_{\downarrow,j,+}(r) \end{pmatrix}, \quad \Psi_{j,-}(r,\phi) = \begin{pmatrix} e^{ij\phi}\, a_{\uparrow,j,-}(r) \\ ie^{i(j-1)\phi}\, b_{\uparrow,j,-}(r) \\ e^{i(j+1)\phi}\, a_{\downarrow,j,-}(r) \\ ie^{ij\phi}\, b_{\downarrow,j,-}(r) \end{pmatrix} \tag{5}$$

Next we combine the radial functions to (normalized) four-spinors

$$\Phi_{j,\tau}(r) = \begin{pmatrix} a_{\uparrow,j,\tau}(r) \\ b_{\uparrow,j,\tau}(r) \\ a_{\downarrow,j,\tau}(r) \\ b_{\downarrow,j,\tau}(r) \end{pmatrix} \tag{6}$$

In this representation, the radial Dirac equation for total angular momentum j and valley index $\tau = \pm$ reads

$$(H_{j,\tau} - E)\, \Phi_{j,\tau}(r) = 0 \tag{7}$$

with Hermitian matrix operators (note that Δ denotes the intrinsic SOI and not the Laplacian)

$$\begin{aligned} H_{j,+} &= \begin{pmatrix} \Delta + V & \nabla_j^{(+)} & 0 & 0 \\ \nabla_{j-1}^{(-)} & -\Delta + V & -\lambda & 0 \\ 0 & -\lambda & -\Delta + V & \nabla_{j+1}^{(+)} \\ 0 & 0 & \nabla_j^{(-)} & \Delta + V \end{pmatrix} \\ H_{j,-} &= \begin{pmatrix} -\Delta + V & \nabla_{j-1}^{(-)} & 0 & -\lambda \\ \nabla_j^{(+)} & \Delta + V & 0 & 0 \\ 0 & 0 & \Delta + V & \nabla_j^{(-)} \\ -\lambda & 0 & \nabla_{j+1}^{(+)} & -\Delta + V \end{pmatrix} \end{aligned} \tag{8}$$

where we use the notation

$$\nabla_j^{(\pm)} = \frac{j}{r} \pm \frac{d}{dr} \tag{9}$$

One easily checks that Equation (8) satisfies the parity symmetry relation

$$H_{-j,\tau} = \sigma_y s_y H_{j,\tau} \sigma_y s_y \tag{10}$$

Note that this "parity" operation for the radial Hamiltonian is non-standard in the sense that the valley is not changed by the transformation $\sigma_y s_y$, spin and sublattice are flipped simultaneously, and only the y-coordinate is reversed. (We will nonetheless refer to $\sigma_y s_y$ as parity transformation below.) A second symmetry relation connects both valleys,

$$H_{j,-\tau} = \sigma_x H_{j,\tau} \sigma_x \tag{11}$$

Using Equation (10), this relation can be traced back to a time-reversal operation. Equations (10) and (11) suggest that eigenenergies typically are four-fold degenerate.

When projected to the subspace of fixed (integer) total angular momentum j, the current density operator has angular component $J_\phi = \sigma_x$ and radial component $J_r = -\tau\sigma_y$ for arbitrary j. When real-valued entries can be chosen in $\Phi_{j,\tau}(r)$, the radial current density thus vanishes separately in each valley. We define the (angular) spin current density as $J_\phi^S = s_z \sigma_x$. Remarkably, the transformation defined in Equation (11) conserves both (total and spin) angular currents, while the transformation in Equation (10) reverses the total current but conserves the spin current. Therefore, at any energy, eigenstates supporting spin-filtered counterpropagating currents are possible. However, in contrast to the edge states found in a ribbon geometry [3], these spin-filtered states do not necessarily have a topological origin.

We focus on one K point ($\tau = +$) and omit the τ-index henceforth; the degenerate $\tau = -$ Kramers partner easily follows using Equation (11). In addition, using the symmetry (10), it is sufficient to study the model for fixed total angular momentum $j \geq 0$.

2.2. Zero Total Angular Momentum

For arbitrary $V(r)$, we now show that a drastic simplification is possible for total angular momentum $j = 0$, which can even allow for an exact solution. Although the lowest-lying bound states for the potentials in Sections 3 and 4 are found in the $j = 1$ sector, exact statements about what happens for $j = 0$ are valuable and can be explored along the route sketched here.

The reason why $j = 0$ is special can be seen from the parity symmetry relation in Equation (10). The parity transformation $\sigma_y s_y$ connects the $\pm j$ sectors, but represents a discrete symmetry of the $j = 0$ radial Hamiltonian $H_{j=0,\tau}$ [see Equation (8)] acting on the four-spinors in Equation (6). Therefore, the $j = 0$ subspace can be decomposed into two orthogonal subspaces corresponding to the two distinct eigenvalues of the Hermitian operator $\sigma_y s_y$. This operator is diagonalized by the matrix

$$U = \frac{1}{\sqrt{2}} \begin{pmatrix} 1 & 0 & 0 & -1 \\ 0 & 1 & 1 & 0 \\ 1 & 0 & 0 & 1 \\ 0 & 1 & -1 & 0 \end{pmatrix} \tag{12}$$

such that

$$U\sigma_y s_y U^{-1} = \mathrm{diag}(1,1,-1,-1) \tag{13}$$

In fact, using this transformation matrix to carry out a similarity transformation, $\tilde{H}_{j,+} = UH_{j,+}U^{-1}$, we obtain

$$\tilde{H}_{j,+} = \begin{pmatrix} \Delta+V & \partial_r & 0 & j/r \\ -1/r-\partial_r & -\Delta+V-\lambda & j/r & 0 \\ 0 & j/r & \Delta+V & \partial_r \\ j/r & 0 & -1/r-\partial_r & -\Delta+\lambda+V \end{pmatrix} \tag{14}$$

For $j = 0$, the upper and lower 2×2 blocks decouple. Each block has the signature ("parity") $\sigma = \pm$ corresponding to the eigenvalues in Equation (13), and represents a mixed sublattice-spin state, see Equations (6) and (12).

For parity $\sigma = \pm$, the 2×2 block matrix in Equation (14) is formally identical to an effective $\lambda = 0$ problem with $j = 0$, fixed $s_z = \sigma$, and the substitutions

$$\Delta \to \Delta + \sigma\lambda/2, \quad E \to E + \sigma\lambda/2 \tag{15}$$

This implies that for $j = 0$ and arbitrary $V(r)$, the complete spectral information for the full Kane–Mele problem (with $\lambda \neq 0$) directly follows from the $\lambda = 0$ solution.

2.3. Solution in Region with Constant Potential

We start our analysis of the Hamiltonian (3) with the general solution of Equation (7) for a region of constant potential. Here, it suffices to study $V(r) = 0$, since E and V enter only through the combination $E - V$ in Equation (8). In Section 3, we will use this solution to solve the case of a step potential.

The general solution to Equation (7) follows from the Ansatz

$$\Phi_j(r) = \begin{pmatrix} c_1 B_{j-1}(\sqrt{p}r) \\ c_2 B_j(\sqrt{p}r) \\ c_3 B_j(\sqrt{p}r) \\ c_4 B_{j+1}(\sqrt{p}r) \end{pmatrix} \tag{16}$$

where the c_i are real coefficients; B_j is one of the cylinder (Bessel) functions; $B_j = J_j$ or $B_j = H_j^{(1)}$; and p denotes a real spectral parameter. In particular, $\sqrt{p}$ is a generalized radial wavenumber. We here assume true bound-state solutions with real-valued energy. However, for quasi-stationary resonance states with complex energy, p and the c_i may be complex as well.

Using the Bessel function recurrence relation, $\nabla_j^{(\pm)} B_j(\sqrt{p}r) = \sqrt{p}B_{j\mp1}(\sqrt{p}r)$, the set of four coupled differential Equations (7) simplifies to a set of algebraic equations

$$\begin{pmatrix} \Delta-E & \sqrt{p} & 0 & 0 \\ \sqrt{p} & -\Delta-E & -\lambda & 0 \\ 0 & -\lambda & -\Delta-E & \sqrt{p} \\ 0 & 0 & \sqrt{p} & \Delta-E \end{pmatrix} \begin{pmatrix} c_1 \\ c_2 \\ c_3 \\ c_4 \end{pmatrix} = 0 \tag{17}$$

Notably, j does not appear here, and therefore the spectral parameter p depends only on the energy E. The condition of vanishing determinant then yields a quadratic equation for p, with the two solutions

$$p_\pm = (E-\Delta)(E-E_\pm), \quad E_\pm = -\Delta \pm \lambda \tag{18}$$

Which Bessel function is chosen in Equation (16) now depends on the sign of $p_\pm$ and on the imposed regularity conditions for $r \to 0$ and/or $r \to \infty$.

For $p_\pm > 0$, a solution regular at the origin is obtained by putting $B_j = J_j$, which describes standing radial waves. Equation (17) then yields the unnormalized spinor

$$\Phi_{j,p_\pm>0}(r) = \begin{pmatrix} \frac{\sqrt{p_\pm}}{E-\Delta} J_{j-1}(\sqrt{p_\pm}r) \\ J_j(\sqrt{p_\pm}r) \\ \mp J_j(\sqrt{p_\pm}r) \\ \mp \frac{\sqrt{p_\pm}}{E-\Delta} J_{j+1}(\sqrt{p_\pm}r) \end{pmatrix} \tag{19}$$

For $p_\pm < 0$, instead it is convenient to set $B_j = H_j^{(1)}$ in Equation (16). Using the identity $H_j^{(1)}(ze^{i\pi/2}) = \frac{2}{\pi i} e^{-ij\pi/2} K_j(z)$, the unnormalized spinor resulting from Equation (17) then takes the form

$$\Phi_{j,p_\pm<0}(r) = \begin{pmatrix} -\frac{\sqrt{-p_\pm}}{E-\Delta} K_{j-1}(\sqrt{-p_\pm}r) \\ K_j(\sqrt{-p_\pm}r) \\ \mp K_j(\sqrt{-p_\pm}r) \\ \mp \frac{\sqrt{-p_\pm}}{E-\Delta} K_{j+1}(\sqrt{-p_\pm}r) \end{pmatrix} \tag{20}$$

where the modified Bessel function $K_j(\sqrt{-p_\pm}r)$ describes evanescent modes, exponentially decaying at infinity.

2.4. Solution without Potential

In a free system, *i.e.*, when $V(r) = 0$ for all r, the only acceptable solution corresponding to a physical state is obtained when $p_\pm > 0$ [30]. For $\Delta < \lambda/2$, at least one $p_\pm > 0$ in Equation (18) for all E, and the system is gapless. However, the TI phase defined by $\Delta > \lambda/2$ has a gap as we show now.

For $\Delta > \lambda/2$, Equation (18) tells us that for $E > \Delta$ and for $E < E_-$, both solutions $p_\pm$ are positive and hence (for given j and τ) there are two eigenstates $\Phi_{j,p_\pm}$ for given energy E. However, within the energy window [with $E_\pm$ in Equation (18)]

$$E_- < E < E_+ \tag{21}$$

we have $p_+ > 0$ and $p_- < 0$, *i.e.*, only the eigenstate Φ_{j,p_+} represents a physical solution. Both $p_\pm$ are negative when $E_+ < E < \Delta$, and no physical state exists at all. This precisely corresponds to the topological gap in the TI phase [3]. Note that due to the Rashba SOI, the valence band edge is characterized by the two energies $E_\pm$, with halved density of states in the energy window (21). One may then ask at which energy (E_+ or E_-) the supercritical diving of a bound state level in an impurity potential takes place.

3. Circular Potential Well

3.1. Bound States

In this section, we study a circular potential well with radius R and depth $V_0 > 0$

$$V(r) = \begin{cases} -V_0, & r < R \\ 0, & r \geq R \end{cases} \tag{22}$$

We always stay within the TI phase $\Delta > \lambda/2$, where bound states are expected for energies $E = E_B$ in the window $\max(\Delta - V_0, E_+) < E_B < \Delta$. For $r < R$, the corresponding radial eigenspinor [see Equation (6)] is written with arbitrary prefactors $A_\pm^<$ in the form

$$\Phi_j^<(r) = \sum_\pm A_\pm^< \Phi_{j,\tilde{p}_\pm}(r) \tag{23}$$

with Equation (19) for $\Phi_{j,\tilde{p}_\pm}(r)$. Here, the $\tilde{p}_\pm > 0$ follow from Equation (18) by including the potential shift,

$$\tilde{p}_\pm = (E + V_0 - \Delta)(E + V_0 - E_\pm) \tag{24}$$

For $r > R$, the general solution is again written as

$$\Phi_j^>(r) = \sum_\pm A_\pm^> \Phi_{j,p_\pm}(r) \tag{25}$$

However, now $\Phi_{j,p_\pm}$ is given by Equation (20), since $p_\pm < 0$ for true bound states with only evanescent states outside the potential well.

The continuity condition for the four-spinor at the potential step, $\Phi_j^<(R) = \Phi_j^>(R)$, then yields a homogeneous linear system of equations for the four parameters ($A_\pm^{<,>}$). A nontrivial solution is only possible when the determinant of the corresponding 4×4 matrix $C(E)$ (which is too lengthy to be given here but follows directly from the above expressions) vanishes

$$\det[C(E)] = 0 \tag{26}$$

Solving the energy quantization condition (26) then yields the discrete bound-state spectrum (E_B). It is then straightforward to determine the corresponding spinor wavefunctions.

Numerical solution of Equation (26) yields the bound-state spectrum shown in Figure 1. When V_0 exceeds a (j-dependent) "threshold" value, V_t, a bound state splits off the conduction band edge. When increasing V_0 further, this bound-state energy level moves down almost linearly, *cf.* inset of Figure 1, and finally reaches the valence band edge $E_+ = -\Delta + \lambda$ at some "critical" value $V_0 = V_c$. (For $j = 0$, we will see below that this definition needs some revision.) Increasing V_0 even further, the bound state is then expected to dive into the valence band and become a finite-width supercritical resonance, *i.e.*, the energy would then acquire an imaginary part.

Figure 1. Bound-state spectrum (E_B) *vs.* Rashba SOI (λ) for a circular potential well with depth $V_0 = 2\Delta$ and radius $R = 3/\Delta$. Only the lowest-energy states with $j = 0, 1, 2$ are shown. The red dotted line indicates $E_+ = -\Delta + \lambda$. The left panel shows $j = 0$ bound states with parity $\sigma = \pm$. The right panel shows $j = 1, 2$ bound states. The inset displays the $j = 1$ bound-state energies *vs.* potential depth V_0 for $\lambda = 0.6\Delta$. At some threshold value $V_0 = V_t$ (where $V_t = 0$ for the lowest state shown), a new bound state emerges from the conduction band. This state dives into the valence band for some critical value $V_0 = V_c > V_t$, where the valence band edge is at energy $E_B = E_+ = -0.4\Delta$. For the second bound state in the inset, V_t (V_c) is shown as red (blue) triangle.

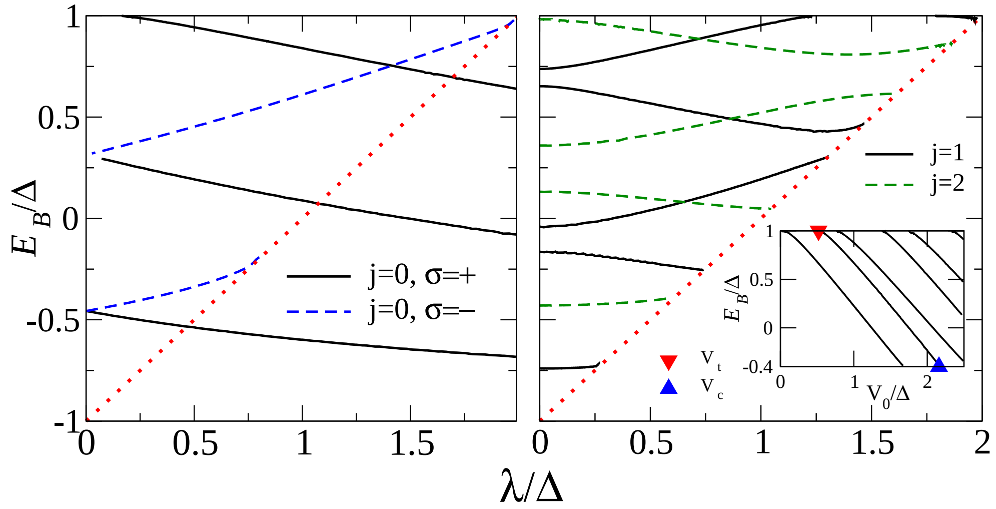

3.2. Zero Angular Momentum States

Surprisingly, for $j = 0$, we find a different scenario where supercritical diving, with finite lifetime of the resonance, happens only for half of the bound states entering the energy window (21). Noting that states with different parity $\sigma = \pm$ do not mix, see Section 2.2, we observe that all $\sigma = +$ bound states enter the valence band as true bound states (no imaginary part) throughout the energy window (21) while the valence band continuum is spanned by the $\sigma = -$ states. We then define V_c for $(j = 0, \sigma = +)$ bound states as the true supercritical threshold where $E_B = E_- = -\Delta - \lambda$. However, the $(j = 0, \sigma = -)$ bound states become supercritical already when reaching $E_+ = -\Delta + \lambda$.

Therefore an intriguing physical situation arises for $j = 0$ in the energy window (21). While $\sigma = +$ states are true bound states (no lifetime broadening), they coexist with $\sigma = -$ states which span the valence band continuum or possibly form supercritical resonances. For $E < E_-$, however, all bound states dive, become finite-width resonances, and eventually become dissolved in the continuum.

3.3. Threshold for Bound States

Returning to arbitrary total angular momentum j, we observe that whenever V_0 hits a possible threshold value V_t, a new bound state is generated, which then dives into the valence band at another potential depth $V_0 = V_c$ (and so on). Analytical results for all possible threshold values V_t follow by expanding Equation (26) for weak dimensionless binding energy $\delta \equiv 1 - E_B/\Delta$. For $\delta \ll 1$ and $j = 1$, Equation (26) yields after some algebra

$$\begin{aligned} \delta &= \frac{2(\hbar v_F/R)^2 e^{-2\gamma}}{\Delta^2\sqrt{1-\tilde{\lambda}^2}} \left(\frac{1-\tilde{\lambda}}{1+\tilde{\lambda}}\right)^{\tilde{\lambda}/2} e^{-\frac{(\hbar v_F/R)^2}{2V_0\Delta}\sum_{\pm} z_\pm J_0(z_\pm)/J_1(z_\pm)} \\ z_\pm &= \sqrt{V_0(2\Delta \pm \lambda + V_0)}R \end{aligned} \tag{27}$$

where $\gamma \approx 0.577$ is the Euler constant and $\tilde{\lambda} = \lambda/2\Delta$. The binding energy approaches zero for $V_0 \to 0$, where Equation (27) simplifies to

$$\delta = \frac{2(\hbar v_F/R)^2}{\Delta^2\sqrt{1-\tilde{\lambda}^2}} \left(\frac{1-\tilde{\lambda}}{1+\tilde{\lambda}}\right)^{\tilde{\lambda}/2} e^{-2\gamma - 2\frac{(\hbar v_F/R)^2}{V_0\Delta}} \tag{28}$$

For vanishing Rashba SOI $\lambda = 0$, this reproduces known results [25]. For any $\lambda < 2\Delta$, we observe that the $j = 1$ bound state in Equation (28) exists for arbitrarily shallow potential depth V_0.

The threshold values V_t for higher-lying $j = 1$ bound states also follow from the binding energy (27), since δ vanishes for $J_1(z_+) = 0$ and for $J_1(z_-) = 0$. When one of these two conditions is fulfilled at some $V_0 = V_t$, a new bound state appears for potential depth above V_t. This statement is in fact quite general: By similar reasoning, we find that the threshold values V_t for $j = 0$ follow by counting the zeroes of $J_0(z_\pm)$. Without SOI, this has also been discussed in [31]. Note that this argument immediately implies that no bound state with $j = 0$ exists for $V_0 \to 0$.

From the above equations, we can then infer the threshold values V_t for all bound states with $j = 0$ or $j = 1$ in analytical form. These are labeled by $n = 1, 2, \ldots$ and $\sigma = \pm$ (for $j = 0$, σ corresponds to parity)

$$V_{t,j,n,\pm} = (\Delta \pm \lambda/2)\left[-1 + \sqrt{1 + \gamma_{j,n}^2/[R(\Delta \pm \lambda/2)]^2}\right] \tag{29}$$

where $\gamma_{j,n}$ is the nth zero of the J_j Bessel function.

Likewise, for $j > 1$, the condition for the appearance of a new bound state is

$$\sum_{\pm}\left[2(j-1)z_\pm J_{j-1}(z_\pm) - \frac{(2\Delta \pm \lambda)V_0}{(\hbar v_F/R)^2} J_j(z_\pm)\right] J_j(z_\mp) = 0 \tag{30}$$

Close examination of this condition shows that no bound states with $j > 1$ exist for $V_0 \to 0$. We conclude that bound states in a very weak potential well exist only for $j = 1$.

3.4. Supercritical Behavior

As can be seen in Figure 1, the lowest $j = 1$ bound state is also the first to enter the valence band continuum for $V_0 = V_c$. For $\lambda = 0$, the critical value is known to be [25]

$$V_c = \Delta\left(1 + \sqrt{1 + \gamma_{0,1}^2/[R\Delta]^2}\right) \tag{31}$$

with $\gamma_{0,1} \approx 2.41$. The energy of the resonant state acquires an imaginary part for $V_0 > V_c$ [25]. For $\lambda > 0$, we have obtained implicit expressions for V_c, plotted in Figure 2. Note that these results reproduce

Equation (31) for $\lambda \to 0$. The almost linear decrease of V_c with increasing λ, see Figure 2, can be rationalized by noting that the valence band edge is located at $E_+ = -\Delta + \lambda$. Thereby supercritical resonances could be reached already for lower potential depth by increasing the Rashba SOI. Similarly, with increasing disk radius R, the critical value V_c decreases, see the inset of Figure 2. For the lowest $(j = 0, \sigma = \pm)$ bound state, the critical value in fact follows in analytical form,

$$V_{c,\sigma=\pm} = (\Delta \pm \lambda/2)\left(1 + \sqrt{1 + \gamma_{1,1}^2/[(\Delta \pm \lambda/2)R]^2}\right) \tag{32}$$

where $\gamma_{1,1} \approx 3.83$.

Figure 2. Critical potential depth V_c for the lowest $j = 1$ bound state level in a disk with $R\Delta = 3$. The obtained $\lambda = 0$ value matches the analytical prediction $V_c \approx 2.28\Delta$ from Equation (31), while $V_c \to 0$ near the border of the TI phase ($\lambda \to 2\Delta$). Inset: V_c *vs*. radius R with several values of λ (given in units of Δ) for the lowest bound state.

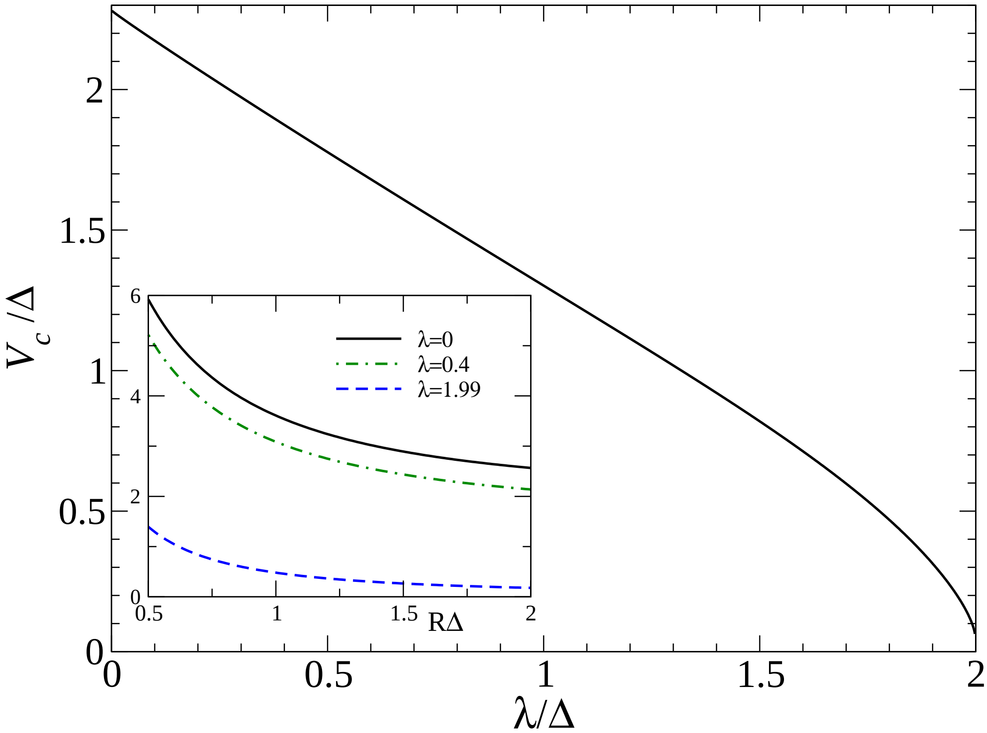

Since the parity decoupling in Section 2.2 only holds for $j = 0$, it is natural to expect that all $j \neq 0$ bound states turn into finite-width resonances when $E_B < E_+$. This expectation is confirmed by an explicit calculation as follows. Within in the window $E_- < E_B < E_+$, a true bound state should not receive a contribution from $\Phi_{j,p_+>0}(r)$ for $r > R$, but instead has to be obtained by matching an Ansatz as in Equation (23) for the spinor state inside the disk ($r < R$) to an evanescent spinor state $\propto \Phi_{j,p_-<0}(r > R)$. However, the matching condition is then found to have no real solution E_B, *i.e.*, there are no true bound states with $j \neq 0$ in the energy window (21). We therefore conclude that all $j \neq 0$ bound states turn supercritical when $E_B < E_+$. Note that this statement includes the lowest-lying bound state (which has $j = 1$). This implies that a finite Rashba SOI can considerably lower the potential depth V_c required for entering the supercritical regime.

4. Coulomb Center

We now turn to the Coulomb potential, $V(r) = -\alpha/r$, generated by a positively charged impurity located at the origin, with the dimensionless coupling strength α in Equation (1). We consider only the TI phase $\Delta > \lambda/2$ and analyze the bound-state spectrum and conditions for supercriticality. Again, without loss of generality, we focus on the K point only ($\tau = +$), and first summarize the known solution for $\lambda = 0$ [2,21,24]. In that case, $s_z = \pm$ is conserved, and the spin-degenerate bound-state energies are labeled by the integer angular momentum j and a radial quantum number $n = 1, 2, 3, \ldots$ (for $j > 0$, $n = 0$ is also possible)

$$E_{j,n}(\lambda = 0) = \Delta \left(1 + \frac{\alpha^2}{\left(n + \sqrt{(j - 1/2)^2 - \alpha^2} \right)^2} \right)^{-1/2} \tag{33}$$

The corresponding eigenstates then follow in terms of hypergeometric functions. The lowest bound state is $E_{j=1,n=0} = \Delta\sqrt{1 - 4\alpha^2}$, which dives when $\alpha = \alpha_c = 1/2$; note that α_c precisely corresponds to V_c in Section 3. In particular, for $(j = 0, \sigma = \pm)$ states we define α_c in the same manner. Next we discuss how this picture is modified when the Rashba coupling λ is included.

Following the arguments in Section 2.2 for $j = 0$, the combination of Equation (33) with Equation (15) immediately yields the exact bound-state energy spectrum ($n = 1, 2, 3, \ldots$)

$$E_{j=0,n,\sigma=\pm} = (\Delta \pm \lambda/2) \left(1 + \frac{\alpha^2}{\left(n + \sqrt{1/4 - \alpha^2} \right)^2} \right)^{-1/2} \mp \lambda/2 \tag{34}$$

The corresponding eigenstates then also follow from [21,24]. The very same reasoning also applies to a regularized $1/r$ potential [23,24], where $V(r < R)$ is replaced by the constant value $V = -\alpha/R$. Here, R is a short-distance cutoff scale of the order of the lattice spacing. The solution of the bound-state problem then requires a wavefunction matching procedure, which has been carried out in [24]. Thereby we can already infer all bound states for $j = 0$.

Figure 3 shows the resulting $j = 0$ bound-state spectrum *vs.* α for the regularized Coulomb potential. Within the energy window Equation (21), we again find that states with parity $\sigma = +$ remain true bound states that dive only for $E_B < E_-$, while $\sigma = -$ states show supercritical diving already for $E_B < E_+$. Figure 4 shows the corresponding critical couplings α_c for $\sigma = \pm$, where the lowest $j = 0$ bound state with parity σ turns supercritical. Note that for finite R and $\lambda \to 0$, a unique value for α_c is found, while for $\lambda \neq 0$ two different critical values for α_c are found. However, this conclusion holds only for finite regularization parameter R, *i.e.*, it is non-universal. As seen in the inset of Figure 4, in the limit $R \to 0$, both critical values for α_c approach $\alpha_c = 1/2$ again, which is the value found without SOI.

Finally, for $j \neq 0$, we can then draw the same qualitative conclusions as in Section 3.4 for the potential well. In particular, we expect that all $j \neq 0$ bound states turn supercritical when their energy E_B reaches the continuum threshold at $E_B = E_+ = -\Delta + \lambda$.

Figure 3. Bound state energies with angular momentum $j = 0$ (E_B in units of Δ) *vs.* dimensionless impurity strength α for the Coulomb problem with regularization parameter $R\Delta = 0.01$ and Rashba SOI $\lambda = 0.6\Delta$. Solid black (dashed blue) curves correspond to parity $\sigma = +$ ($\sigma = -$). Results for radial number $n = 1, 2, 3$ (with increasing energy) are shown. Red dotted lines denote $E = E_\pm$.

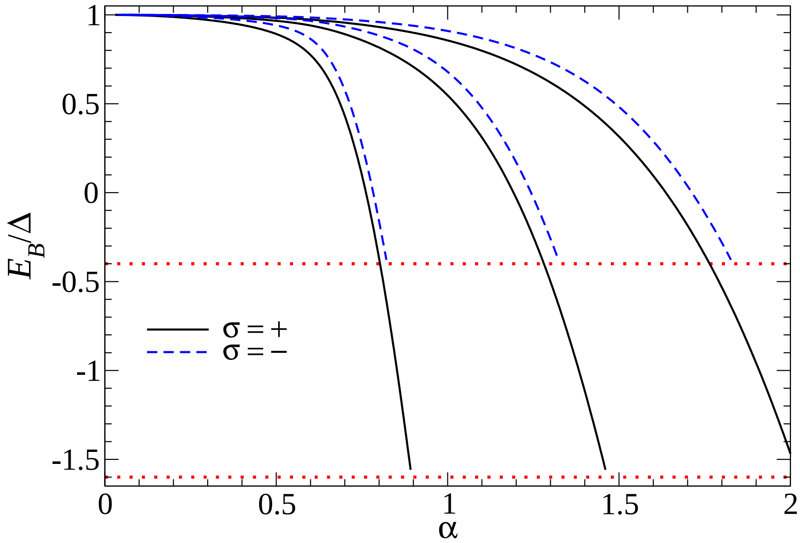

Figure 4. Main panel: Critical Coulomb impurity strength α_c *vs.* Rashba SOI λ for $R\Delta = 0.01$ and the lowest ($j = 0, \sigma = \pm$) bound states. Inset: α_c *vs.* cutoff scale R for $\lambda = 0.6\Delta$.

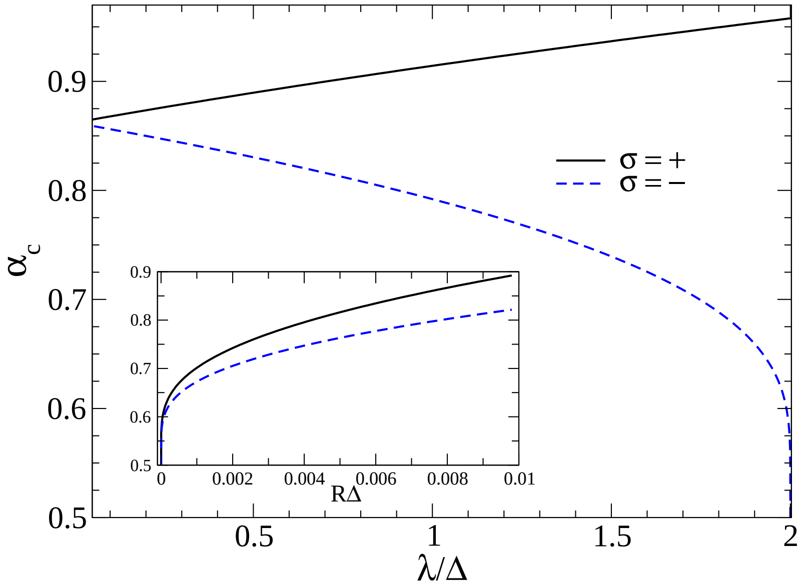

5. Conclusions

In this work, we have analyzed the bound-state problem for the Kane–Mele model of graphene with intrinsic (Δ) and Rashba (λ) spin-orbit couplings when a radially symmetric attractive potential $V(r)$ is present. We have focused on the most interesting "topological insulator" phase with $\Delta > \lambda/2$. The Rashba term λ leads to a restructuring of the valence band, with a halving of the density of states in the window $E_- < E < E_+$, where $E_\pm = -\Delta \pm \lambda$. This has spectacular consequences for total angular momentum $j = 0$, where the problem can be decomposed into two independent parity sectors ($\sigma = \pm$). The $\sigma = +$ states remain true bound states even inside the above window and coexist with the continuum solutions as well as possible supercritical resonances in the $\sigma = -$ sector. However, all $j \neq 0$ bound states exhibit supercritical diving for $E < E_+$, where the critical threshold (V_c or α_c for the disk or the Coulomb problem, respectively) is lowered when the Rashba term is present. We hope that these results will soon be put to an experimental test.

Acknowledgements

This work has been supported by the DFG within the network programs SPP 1459 and SFB-TR 12.

References

1. Castro Neto, A.H.; Guinea, F.; Peres, N.M.R.; Novoselov, K.S.; Geim, A. The electronic properties of graphene. *Rev. Mod. Phys.* **2009**, *81*, 109–162.
2. Kotov, V.N.; Uchoa, B.; Pereira, V.M.; Guinea, F.; Castro Neto, A.H. Electron-electron interactions in graphene: Current status and perspectives. *Rev. Mod. Phys.* **2012**, *84*, 1067–1125.
3. Kane, C.L.; Mele, E.J. Quantum spin hall effect in graphene. *Phys. Rev. Lett.* **2005**, *95*, 226801:1–226801:4.
4. Hasan, M.Z.; Kane, C.L. Topological insulators. *Rev. Mod. Phys.* **2010**, *82*, 3045–3067.
5. Huertas-Hernando, D.; Guinea, F.; Brataas, A. Spin-orbit coupling in curved graphene, fullerenes, nanotubes, and nanotube caps. *Phys. Rev. B* **2006**, *74*, 155426:1–155426:15.
6. Min, H.; Hill, J.E.; Sinitsyn, N.A.; Sahu, B.R.; Kleinman, L.; MacDonald, A.H. Intrinsic and Rashba spin-orbit interactions in graphene sheets. *Phys. Rev. B* **2006**, *74*, 165310:1–165310:5.
7. Yao, Y.; Ye, F.; Qi, X.L.; Zhang, S.C.; Fang, Z. Spin-orbit gap of graphene: First-principles calculations. *Phys. Rev. B* **2007**, *75*, 041401(R):1–041401(R):4.
8. Weeks, C.; Hu, J.; Alicea, J.; Franz, M.; Wu, R. Engineering a robust quantum spin hall state in graphene via adatom deposition. *Phys. Rev. X* **2011**, *1*, 021001:1–021001:15.
9. Shevtsov, O.; Carmier, P.; Groth, C.; Waintal, X.; Carpentier, D. Graphene-based heterojunction between two topological insulators. *Phys. Rev. X* **2012**, *2*, 031004:1–031004:10.
10. Shevtsov, O.; Carmier, P.; Groth, C.; Waintal, X.; Carpentier, D. Tunable thermopower in a graphene-based topological insulator. *Phys. Rev. B* **2012**, *85*, 245441:1–245441:7.
11. Jiang, H.; Qiao, Z.; Liu, H.; Shi, J.; Niu, Q. Stabilizing topological phases in graphene via random adsorption. *Phys. Rev. Lett.* **2012**, *109*, 116803:1–116803:5.
12. Bercioux, D.; de Martino, A. Spin-resolved scattering through spin-orbit nanostructures in graphene. *Phys. Rev. B* **2010**, *81*, 165410:1–165410:9.
13. Lenz, L.; Bercioux, D. Dirac-Weyl electrons in a periodic spin-orbit potential. *Europhys. Lett.* **2011**, *96*, 27006:1–27006:6.
14. Wang, Y.; Brar, V.W.; Shytov, A.V.; Wu, Q.; Regan, W.; Tsai, H.Z.; Zettl, A.; Levitov, L.S.; Crommie, M.F. Mapping dirac quasiparticles near a single coulomb impurity on graphene. *Nat. Phys.* **2012**, *8*, 653–657.

15. Katsnelson, M.I. Nonlinear screening of charge impurities in graphene. *Phys. Rev. B* **2006**, *74*, 201401(R):1–201401(R):3.
16. Pereira, V.M.; Nilsson, J.; Castro Neto, A.H. Coulomb impurity problem in graphene. *Phys. Rev. Lett.* **2007**, *99*, 166802:1–166802:4.
17. Shytov, A.V.; Katsnelson, M.I.; Levitov, L.S. Vacuum polarization and screening of supercritical impurities in graphene. *Phys. Rev. Lett.* **2007**, *99*, 236801:1–236801:5.
18. Shytov, A.V.; Katsnelson, M.I.; Levitov, L.S. Atomic collapse and quasi-rydberg states in graphene. *Phys. Rev. Lett.* **2007**, *99*, 246802:1–246802:5.
19. Biswas, R.R.; Sachdev, S.; Son, D.T. Coulomb impurity in graphene. *Phys. Rev. B* **2007**, *76*, 205122:1–205122:5.
20. Fogler, M.M.; Novikov, D.S.; Shklovskii, B.I. Screening of a hypercritical charge in graphene. *Phys. Rev. B* **2007**, *76*, 233402:1–233402:4.
21. Novikov, D.S. Elastic scattering theory and transport in graphene. *Phys. Rev. B* **2007**, *76*, 245435:1–245435:17.
22. Terekhov, I.S.; Milstein, A.I.; Kotov, V.I.; Sushkov, O.P. Screening of coulomb impurities in graphene. *Phys. Rev. Lett.* **2008**, *100*, 076803:1–076803:4.
23. Pereira, V.M.; Kotov, V.N.; Castro Neto, A.H. Supercriticial coulomb impurities in gapped graphene. *Phys. Rev. B* **2008**, *78*, 085101:1–085101:8.
24. Gamayun, O.B.; Gorbar, E.V.; Gusynin, V.P. Supercritical coulomb center and excitonic instability in graphene. *Phys. Rev. B* **2009**, *80*, 165429:1–165429:14.
25. Gamayun, O.B.; Gorbar, E.V.; Gusynin, V.P. Magnetic field driven instability of a charged center in graphene. *Phys. Rev. B* **2011**, *83*, 235104:1–235104:9.
26. Zhu, J.L.; Sun, S.; Yang, N. Dirac donor states controlled by magnetic field in gapless and gapped graphene. *Phys. Rev. B* **2012**, *85*, 035429:1–035429:9.
27. Huertas-Hernando, D.; Guinea, F.; Brataas, A. Spin-orbit mediated spin relaxation in graphene. *Phys. Rev. Lett.* **2009**, *103*, 146801:1–146801:4.
28. Rashba, E.I. Graphene with structure-induced spin-orbit coupling: Spin-polarized states, spin zero modes, and quantum Hall effect. *Phys. Rev. B* **2009**, *79*, 161409(R):1–161409(R):4.
29. De Martino, A.; Hütten, A.; Egger, R. Landau levels, edge states, and strained magnetic waveguides in graphene monolayers with enhanced spin-orbit interaction. *Phys. Rev. B* **2011**, *84*, 155420:1–155420:12.
30. Rakyta, P.; Kormanyos, A.; Cserti, J. Trigonal warping and anisotropic band splitting in monolayer graphene due to Rashba spin-orbit coupling. *Phys. Rev. B* **2010**, *82*, 113405:1–113405:4.
31. Bardarson, J.H.; Titov, M.; Brouwer, P.W. Electrostatic confinement of electrons in an integrable graphene quantum dot. *Phys. Rev. Lett.* **2009**, *102*, 226803:1–226803:4.

© 2013 by the authors; licensee MDPI, Basel, Switzerland. This article is an open access article distributed under the terms and conditions of the Creative Commons Attribution license (http://creativecommons.org/licenses/by/3.0/).